Third glare point effect in 90°Interferometric Laser Imaging for Droplet Sizing

Justin Jacquot, Mohamed Talbi, Marc Brunel

Third glare point effect in 90° Interferometric Laser Imaging for Droplet Sizing

Justin JACQUOT-KIELAR [1,2], Mohamed TALBI [1], Marc BRUNEL [1]

[1] : UMR 6614 – CORIA, Normandie Université, CNRS, Université et INSA de Rouen, BP 12, 76801 Saint-Etienne-du-Rouvray, France

[2] : Department of Earth, Atmospheric and, Planetary Sciences, Purdue University, 550 Lafayette St, West Lafayette, IN 47907, USA

Abstract

A detailed analysis of Interferometric Laser Imaging for Droplet Sizing is performed at the scattering angle 90°, in order to identify the influence of a third glare point on the measurements performed. Experimentally, p=3 scattering, which involves surface waves, is shown to have an important impact on droplet sizing.

1. Introduction

Interferometric out-of-focus imaging is a promising technique to measure the size of droplets and ice particles in the atmosphere. A laser beam crosses the particle's path. A defocused imaging system records 2-dimensional interference patterns due to light scattered by the particles. The fringe frequency delivers the size of the droplets [1-12]. While water droplets typically produce two-wave interference patterns, ice particles give speckle-like patterns that can be analysed [13-15]. Mixed conditions, as freezing droplets can be observed as well : the droplet's glare points [16] break then into a high number of secondary emitters [17].

In the case of liquid water droplets, the expected two-wave interference pattern is produced by the interference between the part of light reflected on the particle and the part of light refracted in the particle (the p=0 and p=1 orders using a Debye series expansion [18]). An optimized contrast of the fringes is observed at the specific scattering angle of 67° for water droplets in air, with a perpendicular polarization of the incident laser light. This configuration leads to an optical arrangement of all elements that can be relatively complex and cumbersome, as with the ALIDS probe [12]. A second solution is to realize a system with a scattering angle of 90° under parallel polarization of the laser light [19-21]. The whole system can then be significantly smaller. In addition, the configuration of ILIDS at 90° enables the installation of the technique around parallelepipedic sections of Wind Tunnels, while the configuration at 67° would induce significant optical aberrations.

Although geometrical optics cannot fully explain the refracted beam in this configuration at 90° [22], wave optics theories show that well-contrasted two-wave interference patterns are observed with water droplets. At the same time, the size of ice particles can be estimated from the analysis of their speckle patterns [21].

Nevertheless, the description of the light scattering process is more complex at this specific scattering angle of 90°. In the worst case, it appears that the interpretation of interferometric images can cause an erroneous estimation of the droplet's size. In this paper, we present experimental results showing that a wrong size estimation can occur, due to the combination of the presence of a third glare point and of a non-uniform illumination of the droplet.

Section 2 is a theoretical section in order to better understand some effects that can occur. Section 3 will present the experimental set-up. Section 4 will show experimental results. The influence of a third glare point will be detailed. We will show that it must be taken into account for proper interpretation of the results. In most cases, it does not prevent particle sizing. However, combined to a non-uniform illumination of the droplet, we will show the possibility of erroneous measurement.

2. Theory

Light scattered by the droplets can be described rigorously using the generalized Lorenz-Mie theory. In this case of interferometric particle imaging experiments, a theoretical description that uses a Debye series expansion is very useful since it establishes indeed a link with geometrical optics, and evidences the rays that take part to the scattering process (depending on the scattering angle and the polarization state of the laser).

Let us consider a spherical water droplet of radius 80 μm (real part of the refractive index n=1.3363, imaginary part k=1.8 10^{-9}). It is illuminated by a coherent plane wave of wavelength 532nm, under parallel polarization. Using the Debye series decomposition, it is possible to calculate the intensity of the light scattered versus the scattering angle. To do this, we use the MiePlot software developed by Philip Laven [23]. Figure 1 presents the intensity of all scattering orders p=0 to p=7 versus the scattering angle θ in the range [60°,120°]. The y-axis is in logarithmic scale because the intensity of some orders can be very low. For example, the intensity of order p=2 is so low that it does not appear on the figure. Let us consider the scattering angle θ=90° that will be used in this paper. It appears clearly that two orders dominate : p=0 (reflected ray) and p=1 (transmitted ray without any internal reflection). Order p=3 is less important and other orders are lower. For an easier interpretation, figure 2 shows a geometrical representation of main orders p=0, p=1 and p=3. The relatively high-intensity of order p=1 is actually not obvious. Using geometrical optics, the p=1 ray can exist only if the scattering angle θ does not exceed 83.1° (for a water droplet of index n=1.3363 as in present study). Nevertheless, figure 1 shows that order p=1 has a non-zero intensity at θ=90°. This is due to surface waves that contribute to scattering

(as shown diagrammatically on figure 2 that includes a curved ray representing surface waves traveling along 6.9° of the particle's circumference before "exiting" in B). The importance of such surface waves on the scattering process has been evidenced in different studies in the past [24]. We can further note on figure 2 that two paths exist for p=3, which will be discussed later.

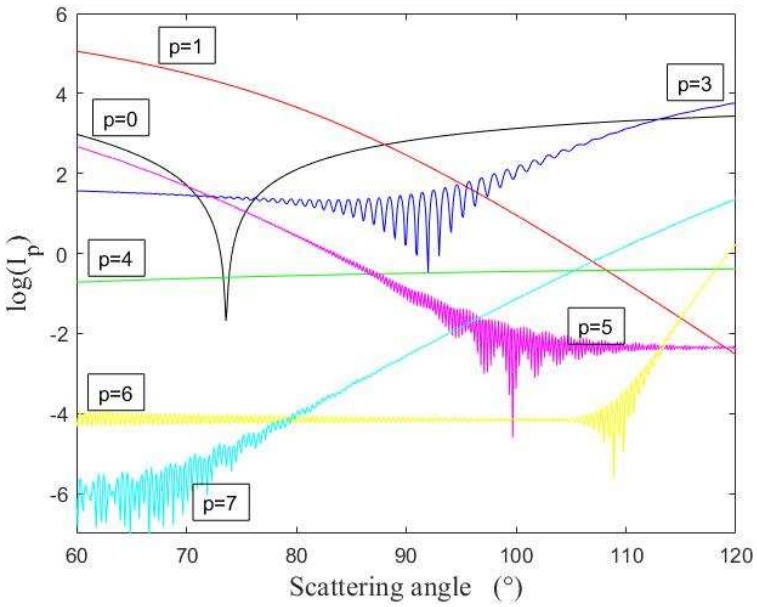

Figure 1 : intensity of scattering orders p=0 to p=7 versus the scattering angle θ for a water droplet of radius 80 µm. (The intensity of order p=2 is lower and does not appear).

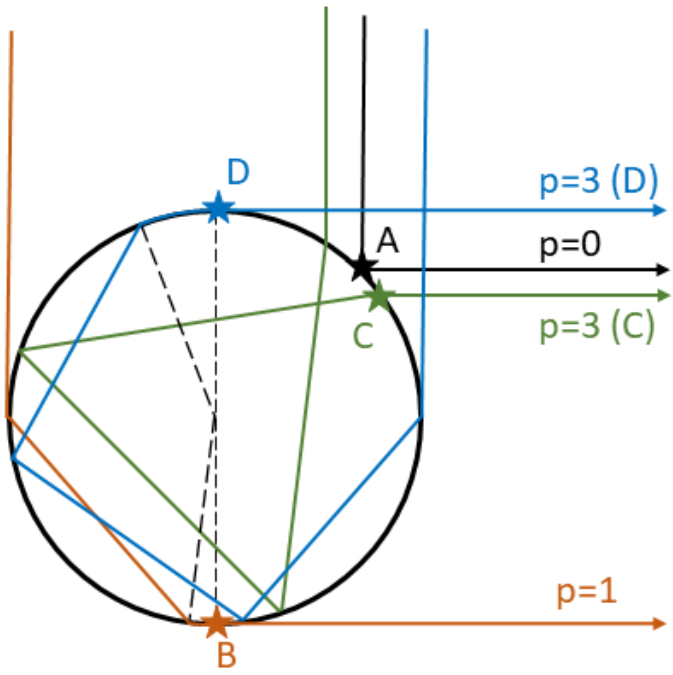

Figure 2 : schematic representation of the four glare points A, B, C and D corresponding to scattering orders p=0 (A), p=1 (B) and p=3 (C and D).

The plot of figure 1 tends to confirm that we should observe well-contrasted two-wave interference fringes using the ILIDS set-up in this configuration. Nevertheless, order p=3 is not low enough to be considered as fully negligible. Order p=3 seems to be more significant than expected and might have a role to play. Let us discuss this point more deeply. Figure 3 shows now two scattering diagrams, limited to orders p=0, 1 and 3 (we have verified that these orders dominate in these new cases), and the scattering angle is reduced to the range [80° ; 100°]. The radius of the water droplet is 15 μm in the case (a) and 80 μm in case (b).

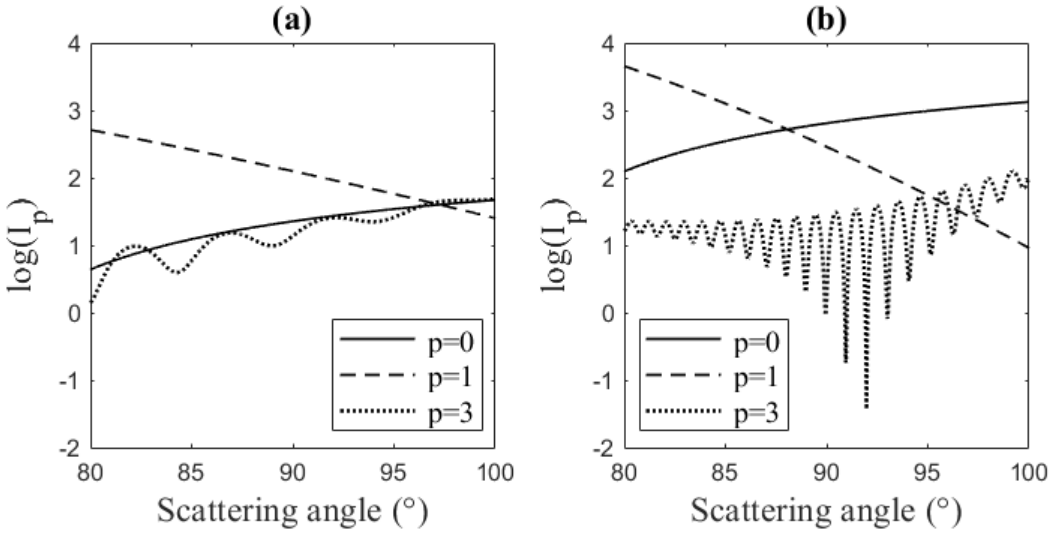

Figure 3 : intensity of scattering orders p=0, p=1 and p=3 versus the scattering angle θ for water droplets of radii 15 μm (a) and 80 μm (b).

This second diagram brings very important information :

- For small particles (case (a)), orders p=0 and p=3 have similar intensities. It can induce a confusion when estimating the size of the particle.
- In both cases ((a) and (b)), when the scattering angle reaches 95°, the intensity of order p=3 can become comparable or higher than the intensity of order p=1.
- Order p=3 shows oscillations between θ = 80° and θ = 100°. For example, in case (a), the intensity of order p=3 is higher than the intensity of order p=0 at angle 82°, but significantly lower at angle 84°. The oscillations are actually due to the interferences between two optical paths, both corresponding to order p=3. These two paths are presented on figure 2 and lead to the existence of two glare points C and D. The path corresponding to glare point C is a classical geometrical ray, while the path corresponding to glare point D involves surface waves along about 21° of the particle's circumference. It might be assumed that the intensity of this latter path is much weaker but the contrast of the oscillations between θ=85° and θ=98° shows

that this assumption is not verified : the contrast shows indeed that both paths are present in this range of scattering angle and interfere. In figure 3(b) for 80µm droplets, the maximum contrast for p = 3 scattering occurs near θ=92°, indicating that the two p = 3 paths have similar amplitudes at this scattering angle. Glare point C due to a classical geometrical ray is actually dominant when θ < 92°, while glare point D due to surface waves becomes dominant when θ > 92°. But the contrast of the oscillations shows that glare point D is never fully negligible.

Two reasons explain the importance of these latter remarks :

- In ILIDS, the imaging set-up has a non-zero aperture. It means that the light collected by the imaging system corresponds to a range of scattering angles (rather than the median value 90°) : for example [88°,92°] using a low aperture system, or [80°,100°] using a very large aperture system. The intensity of all scattered orders has thus to be integrated over the whole range of scattering angles authorized by the aperture.
- The droplet is not necessarily on the optical axis of the imaging system. The field of view in ILIDS is indeed large. It means that depending on the transverse position of the droplet in the laser sheet, the range of scattered angles to be considered for a low aperture system can be [86°,90°], [88°,92°], or [90°,94°]. This point is illustrated on figure 4 that shows the range of scattering angles that have to be considered depending on the position of the droplet.

In addition to both previous deterministic arguments, it must be kept in mind that an ILIDS set-up can suffer misalignments (of the laser sheet or of the imaging set-up), which adds a further uncertainty on the determination of the range of scattering angles that have to be considered to interpret the interferometric images and their interference patterns.

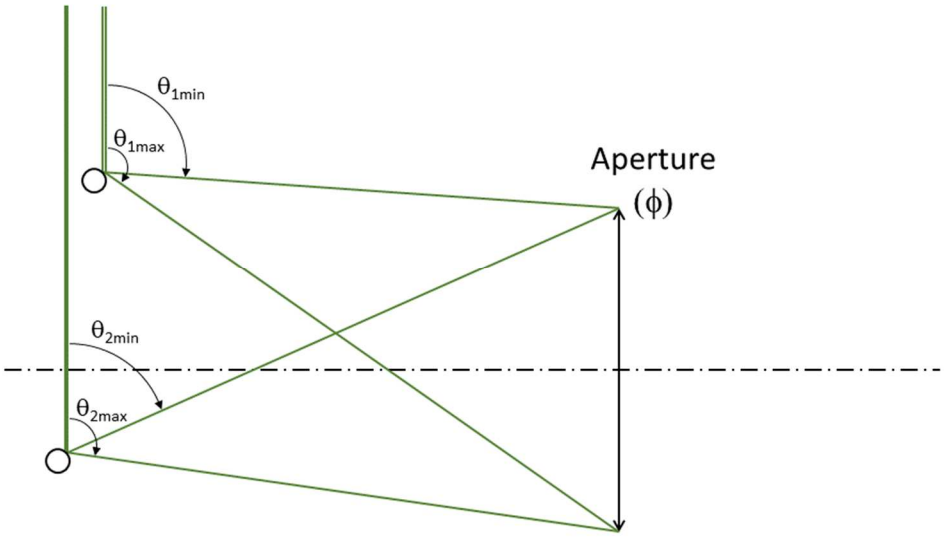

Figure 4 : range of scattering angles to be considered depending on the position of the droplet in the field of view. Two cases are illustrated here : droplet over the optical axis (range $[\theta_{1min}; \theta_{1max}]$), or below the optical axis (range $[\theta_{2min}; \theta_{2max}]$).

In summary, figure 1 by itself is not sufficient to prove that only orders p=0 and p=1 have to be considered in this 90°-configuration of ILIDS. As order p=3 could have significant consequences, it requires a deeper investigation. Figure 5 compares these two configurations :

- in black is reported the intensity of scattering orders p=0 (star), p=1 (cross) and p=3 (circles) versus the droplet's radius. In all three cases, the intensity is integrated over the range of scattering angles [87°,93°]. It appears clearly that the two main orders are p=0 and p=1 for all droplet's radii. For a small droplet (radius 15 µm), the intensity of order p=3 approaches the intensity of order p=1. Nevertheless, the classical ILIDS analysis seems to be achievable according to these three plots, although the contrast of the fringes should not be always optimum.
- In red is reported the intensity of scattering orders p=0 (star), p=1 (cross) and p=3 (circles) versus the droplet's radius. In all three cases, the intensity is integrated over the range of scattering angles [93°,99°]. The very important point is that for big droplets (radius higher than 100 µm, the intensity of order p=3 becomes larger than the one of order p=1. This fact can have important consequences in size determination.

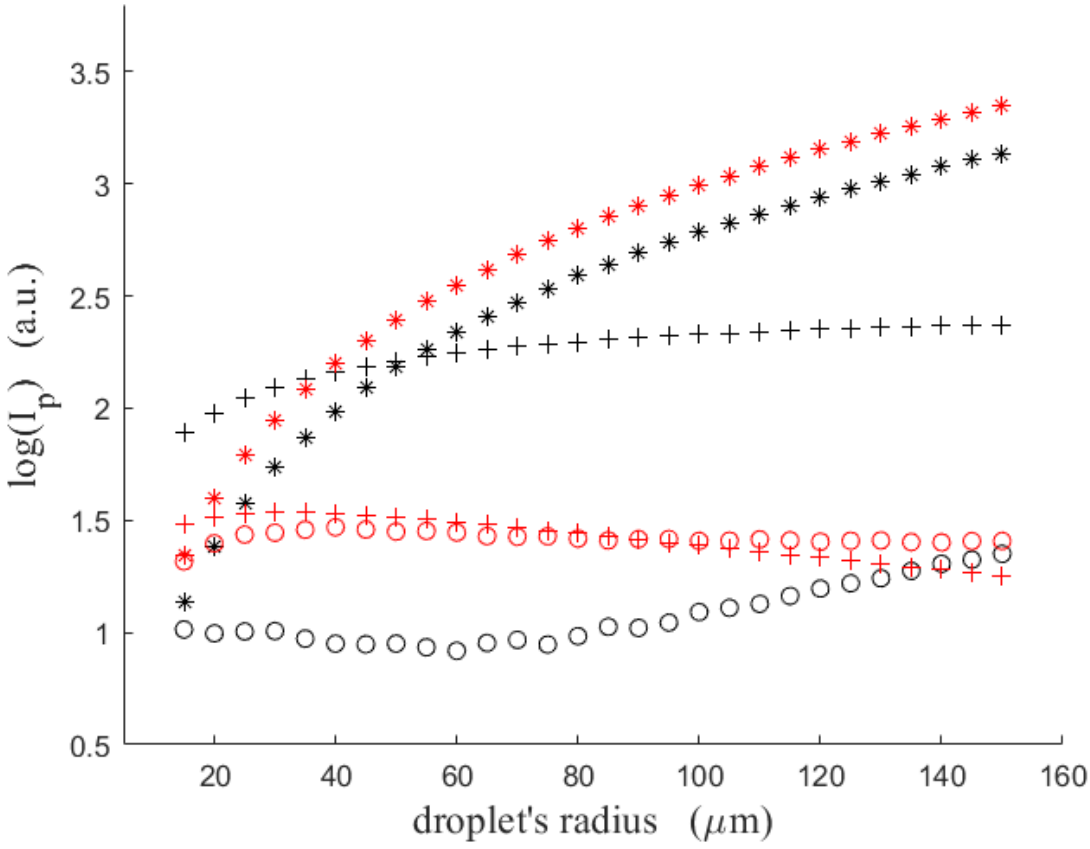

Figure 5 : intensity of scattering orders p=0 (star), p=1 (cross) and p=3 (circles) versus the droplet's radius. In black, the intensity has been integrated over the range of scattering

angles [87°,93°]. In red, the intensity has been integrated over the range of scattering angles [93°,99°].

In order to better understand these consequences, it is helpful to refer to figure 2 which shows a geometrical representation of scattered orders p=0, 1 and 3. If the intensities of orders p=0 and p=1 are much higher than the intensities of all other orders, the ILIDS pattern will be composed of a two-wave interference pattern emitted by the two glare points A and B. The fringe frequency will be proportional to the distance separation between A and B. If the intensity of order p=3 is not negligible, the ILIDS pattern will be composed of a three- or four-wave interference pattern, emitted by glare points A, B, C and/or D. The analysis will be slightly more difficult but it remains possible, as could be done with bubbles [25]. But if the intensity of order p=1 becomes negligible in front of the intensity of order p=3, the ILIDS pattern will be composed of an interference pattern emitted by glare points A and C (and/or D). In this case, the size determination will be wrong if the pattern is interpreted as produced by glare points A and B. As A, C and D are close to each other, whereas A and B are widely separated, incorrect assumptions can lead to a huge error.

Next section will present experimental results where such an error is observed.

3. Experimental set-up

Figure 6 shows the experimental setup used for this study. Water droplets are generated by a plant sprayer. It generates droplets whose diameter is in the range [40 ; 400 μm]. The droplets fall in a column at ambient temperature. Imaging experiments are performed at the bottom of the column through glass windows (BK7). The interferometric out-of-focus imaging setup is composed of a frequency-doubled Nd :YAG laser emitting 20mJ, 4ns, 532nm pulses. A laser sheet is formed in the center of the column by the combination of cylindrical and spherical lenses. The thickness of the laser sheet is about 1.5mm. Experiments are performed using a parallel polarization of the laser light (with respect with the incidence plane of the droplets, as in the theoretical part). The field scattered by the droplets is collected at a scattering angle θ of 90° to realize the interferometric particle imaging experiments. For proper validation of the IPI analysis, out-of-focus imaging and in-focus imaging are realized simultaneously. This is performed using a beam splitter, two imaging lines and two cameras. Light reflected by the beam splitter is collected by the in-focus optical system, while light transmitted is collected by the out-of- focus setup. In-focus imaging uses a far-field objective provided by ISCOOPTIC (field of view : 2.6mmx2.6 mm). The out-of-focus system consists of a Nikon objective (focus length of 200mm). Defocus is obtained adding an extension tube. Both sensors are 2048x2048pixels CCD sensors (pixel size of 5.5 μm). Images are recorded in 12 bits at a 25 frames per second rate. An external electronic device allows a perfect synchronization of the CCD sensors with the laser pulses.

The out-of-focus imaging part of the system is described as follows: the CCD sensor is 11.2 mm large ($2048 \times 5.5\mu m$). The distance from the object (the droplets) to the Nikon objective is approximately 400mm, while the distance from the objective to the CCD sensor is around 450mm. It means that the region of interest in the object's plane is approximately a square of dimension $10mm \times 10mm$. The aperture number is 4.7, indicating a diameter of the entrance pupil of 42 mm. Depending on the position of the droplet (below the optical axis, or over the optical axis according to figure 4 of previous section), the range of scattering angles to be considered in these experiments can be from [86.3° ; 92.3°] to [87.7°,93.7°]. Any additional misalignment of the system or of the laser sheet will increase the range of scattering angles.

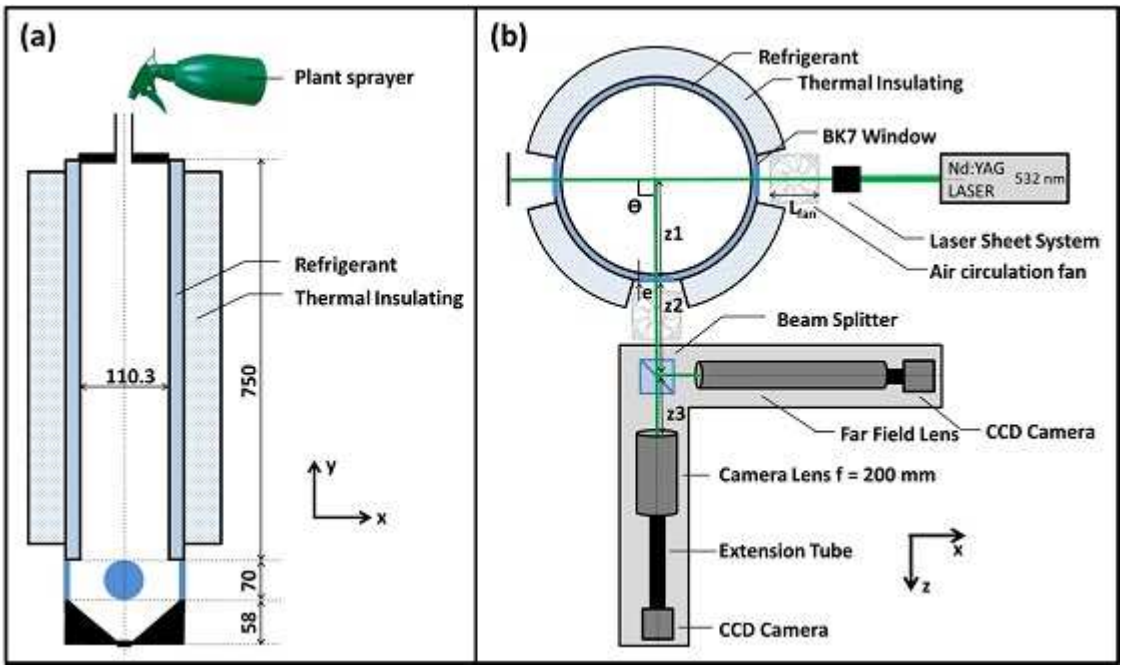

Figure 6 : experimental set-up : (a) side-view, (b) top view.

The quantitative analysis of the out-of-focus images requires the determination of the optical transfer matrix describing the system from the laser sheet to the CCD sensor [8]. Each element of the optical system corresponds to a matrix T_n. The total transfer matrix can be written according to: $M_{tot} = T_n \times T_{n-1} \times \ldots \times T_1$. In the case of our experiment, the analytical expression of the total transfer matrix is given by:

$$M_{tot} = \begin{bmatrix} A_{tot} & B_{tot} \\ C_{tot} & D_{tot} \end{bmatrix} = \begin{bmatrix} 1 - \frac{z_4}{f} & z_{eq} + z_4 - \frac{z_{eq}\ z_4}{f} \\ -\frac{1}{f} & 1 - \frac{z_{eq}}{f} \end{bmatrix}$$

where $z_{eq} = z_1 + z_2 + z_3 + \frac{e_1 + e_2}{n_2}$ and f is the focus length of the Nikon objective (200mm) [21]. Fig. 6 describes the setup. The distance from the particle to the window of the column

is z_1. The NBK7 window has a thickness e_1 and is located at a distance of z_2 to the front surface of the beam splitter. The beam splitter is a NBK7 cube of thickness e_2. The distance between the rear face of the beam splitter and the objective is z_3 while z_4 is the distance between the lens and the CCD sensor. The experimental parameters of the set-up are indicated below: z_1 = 79.5 mm, e_1 =3 mm, z_2 = 132.5 mm, e_2 = 25.4 mm, z_3 = 161 mm, z_4 = 452 mm. According to the optical arrangement, the total transfer matrix coefficient B_{tot} is estimated to be $-0.0416\ m$.

4. Experimental results

4.1. General case

Figure 7(a) shows the interferometric out-of-focus image of a water droplet recorded with this setup. It corresponds to a typical image that is observed in many cases. Figure 7(b) shows the intensity of a central horizontal pixel line of the interferometric image. The pattern observed corresponds to a three-wave interference pattern. To simplify, a high frequency component due to glare points A and B is observed. It is modulated by a low-frequency component due to nearby glare points A and C or D. This is confirmed by the in-focus image of the same droplet recorded simultaneously with the in-focus imaging line. It is presented in figure 8(a) without contrast adjustment, and in figure 8(b) after contrast adjustment (in order to improve the intensity of glare point B). We observe the presence of three glare points, as could be expected theoretically. This image shows clearly that a third glare point is not negligible. Note that such a case is frequently observed in our experiments, as will be detailed in the next sections. With our experimental set-up, the range of scattering angles to be considered in the experiments can vary from [86.3° ; 92.3°] to [87.7°,93.7°]. According to the comments of theoretical section 2, it means that both glare points C and D could have non negligible amplitudes, and give rise to a three- or four-waves interference pattern. Let us consider figure 8 more deeply, the position of the three spots observed, and their relative intensities tend to indicate that the right hand-sided spot corresponds to glare point B while the left-hand sided spot corresponds to glare point D. The intense inner spot is attributed to glare point A, corresponding to the reflected part of the beam (probably slightly spread by a combination with glare point C).

Quantitatively, let us first consider the interferometric pattern of figure 7. The low frequency is measured using figure 7(b). The low-frequency interfringe is estimated to be 191 pixels. As the size of each pixel of the sensor is 5.5 µm, the interfringe of this low-frequency component is 1.05mm, which gives a fringe frequency $\nu_\ell = 0.952\ mm^{-1}$. The wavelength of the laser is $\lambda\ = 532\ nm$, while the matrix transfer coefficient B_{tot} has been estimated to be -0.0416m in this configuration. The distance between the two nearby glare points responsible for the low-frequency component of the pattern is thus $d_{AD} = |\lambda\, B_{tot}\, \nu_\ell| =$

$22\ \mu m$. The highest frequency is measured using the same figure 7(b). The high-frequency interfringe is estimated to be 28 pixels, which gives 154 µm, and thus a highest frequency $\nu_h = 6.5\ mm^{-1}$. The distance between the two farthest glare points is thus $d_{BD} = |\lambda\ B_{tot}\ \nu_h| = 143\ \mu m$.

Let us now consider the in-focus image of figure 8. It is presented in figure 8(a) without contrast adjustment, and in figure 8(b) after contrast adjustment. The pixel size of the in-focus CCD sensor is 5.5 µm. The in-focus imaging system introduces a magnification factor $g = -4.33$. Each pixel on the images of figure 8 represents thus a distance of 1.27 µm in the plane of the object, i.e. the plane of the glare points A, B, and D. On figure 8, we measure a distance between the nearby glare points A and D of 18 pixels on the sensor, i.e. $d_{AD} = 23\mu m$ on the droplet. The distance between glare points B and D is 115 pixels on the sensor, i.e. $d_{BD} = 146\mu m$ on the droplet. Both analyses made from direct in-focus imaging and interferometric out-of-focus imaging correspond quantitatively well.

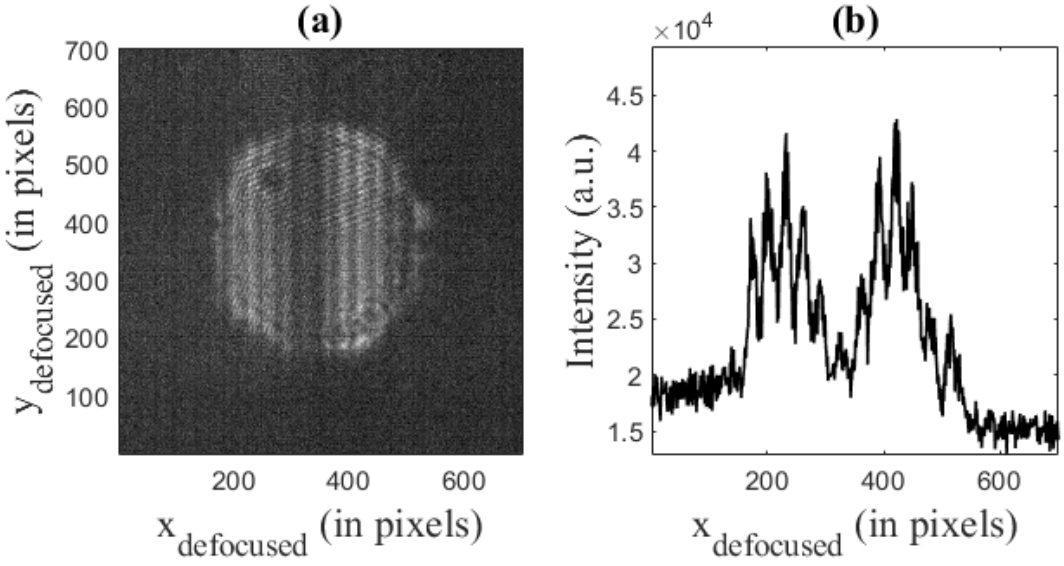

Figure 7 : interferometric out-of-focus image of a droplet (a) and the intensity of a central horizontal pixel line of the interferogram (b)

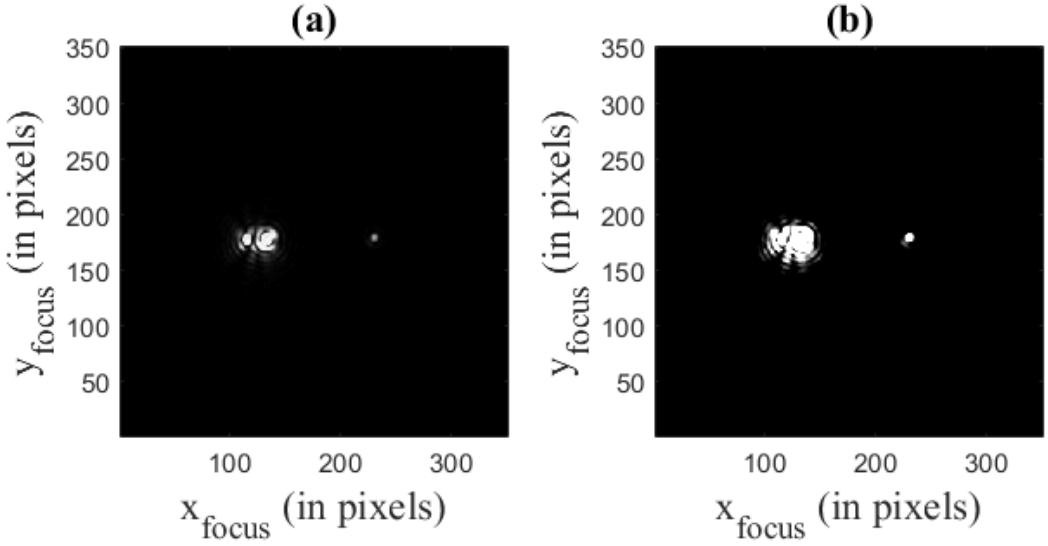

Figure 8 : glare points of the droplet whose defocused image is reported in figure 7(a), without contrast enhancement (a) and after contrast enhancement (b).

4.2. Special case

Figure 9(a) shows the interferometric out-of-focus image of another droplet recorded with the same set-up. Figure 9(b) shows the intensity of a central horizontal pixel line of the interferometric image. The pattern observed corresponds to a two-wave interference pattern. There is only a low frequency component. Quantitatively indeed, the interfringe measured on figure 9(b) is 174 pixels. As the size of each pixel of the sensor is 5.5 µm, the interfringe is 957 µm, which gives a fringe frequency $v = 1.044\, mm^{-1}$. As in previous section, the laser wavelength is $\lambda = 532\, nm$, and parameter B_{tot} equals -0.0416m in this configuration. The distance between the two glare points responsible for the pattern is thus $|\lambda\, B_{tot}\, v| = 23\mu m$. If the fringes are attributed to glare points A and B, then we conclude that it is a small droplet.

But this is not confirmed by the in-focus image of the same droplet that has been recorded simultaneously. It is presented in figure 10(a) without contrast adjustment, and in figure 10(b) after contrast adjustment (in order to improve the intensity of the real glare point B). If figure 10(a) shows only two glare points that explain the interferometric pattern of figure 9, figure 10(b) shows that there are actually three glare points, as in previous section. Nevertheless, the intensity of glare point B is much lower than the intensity of glare points A and D. The result is that the presence of a high frequency component is hidden in the noise of the interferometric pattern of figure 9. The consequence is a possible false estimation of the size of the droplet. As in previous section, the pixel size of the in-focus CCD sensor is 5.5 µm. The in-focus imaging system introduces a magnification factor $g = -4.33$. Each pixel on the images of figure 10 represents 1.27 µm in the plane of the object, i.e. the plane of the

glare points A, B and D. Figures 10(a) and 10(b) show that the distance between the nearby glare points A and D is 19 pixels on the sensor, i.e. 24µm on the droplet. But the distance between glare points A and B is 96 pixels on the sensor, i.e. 122µm on the droplet. The real distance between glare points B and D is actually 146 µm, which corresponds to a relatively big droplet. This case shows clearly that p=3 scattering is clearly not negligible. This is a typical error observed from time to time during our experiments.

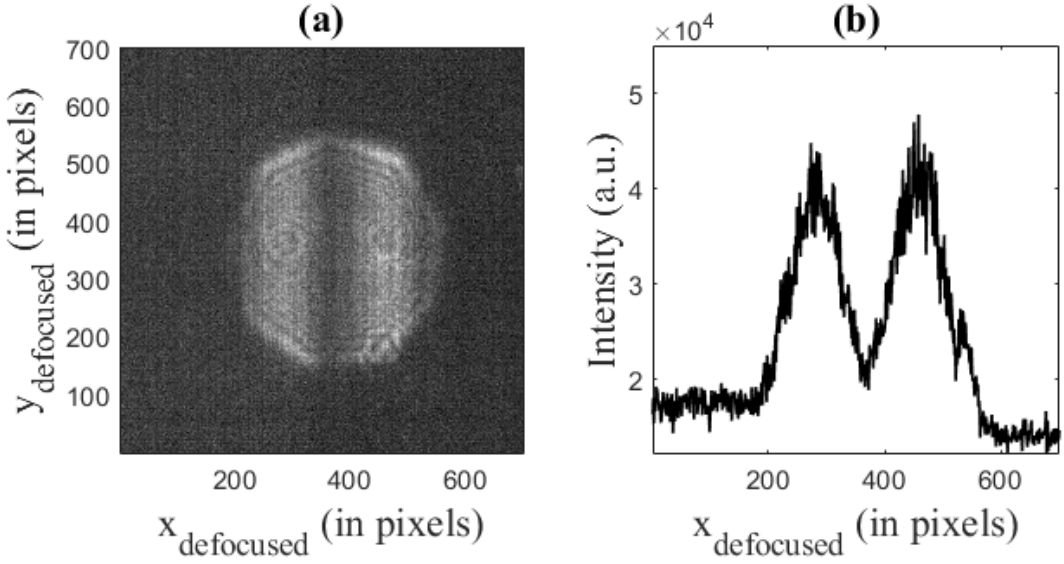

Figure 9 : : interferometric out-of-focus image of a droplet (a) and the intensity of a central horizontal pixel line of the interferogram (b)

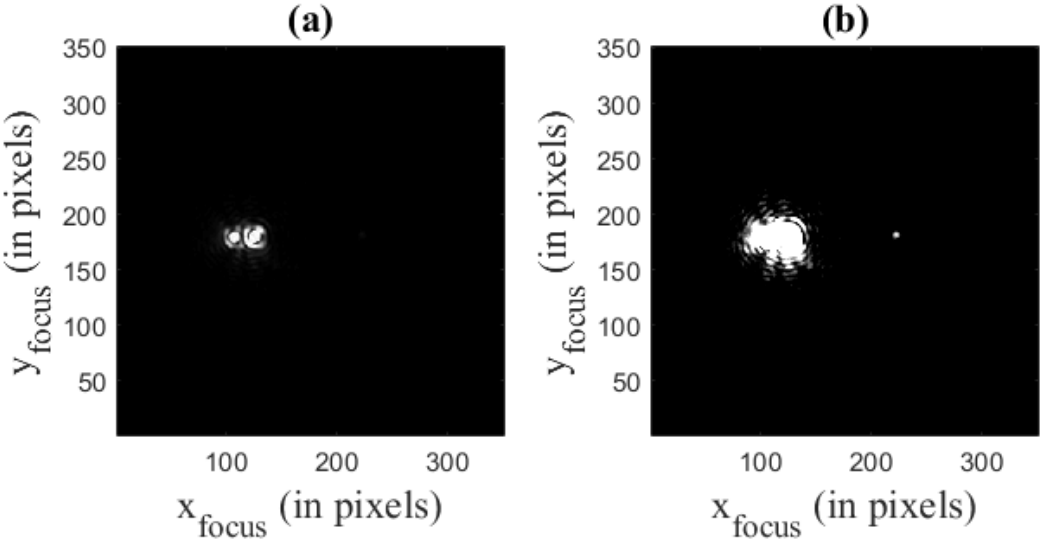

Figure 10 : glare points of the droplet whose defocused image is reported in figure 7(a), without contrast enhancement (a) and after contrast enhancement (b).

4.3. Glare points observation of different droplets

In order to estimate the probability of erroneous interpretations, figure 11 shows 9 in-focus images of different water droplets recorded with the same previous setup. The axes of all images are in pixels. The in-focus system has not been modified : pixel size of the CCD sensor of 5.5 µm, magnification factor introduced $g = -4.33$. Each pixel on the images of figure 11 represents thus a distance of 1.27 µm in the plane of the objects (i.e. the glare points A, B and D). Table 1 summarizes the distances recorded between glare points B and D (noted d_{BD}), and between glare points A and B (noted d_{AB}) for all cases (a) to (i) of figure 11. The ratio d_{AB}/d_{BD} is calculated in the last column of Table 1. Obviously, the mean value is 0.855 with a very low difference among the reported values. As B and D are due to surface waves, BD is a diameter of the droplet (see figure 2) such that $d_{droplet}=d_{BD}$. In the same time, the height of point A is given geometrically by $d_{AB} = \frac{d_{droplet}}{2}\left(1 + \cos\left(\frac{\pi}{4}\right)\right) \simeq 0.853\ d_{droplet}$ for a scattering angle of 90°. We can note that the value 0.853 corresponds to ratio d_{AB}/d_{BD} reported in all cases of Table 1, which tends to confirm the attribution of the spots observed to optical paths that define A, B and D. Let us now discuss the different cases reported in figure 11 :

- Figures 11(a), 11(b) and 11(c) show cases where the intensity of glare point D is much lower than the intensity of glare points A and B. D appears indeed on these figures after a combination of huge contrast enhancement. The consequence on ILIDS analysis is the observation of a two-wave interference pattern. The fringe frequency is due to glare points A and B and gives d_{AB}. The diameter of the particle should then be deduced from relation $d_{droplet} = d_{AB}/0.853$.

- In the case of figure 11(d-i), the intensity of three glare points is such that a three-wave pattern is recognized and a proper estimation of the droplet's size can be done. However, some cases show that the intensity of glare point D can be comparable to the intensities of glare points A and B. The analysis is feasible, as in the case discussed in figures 7 and 8, with a better contrast of the high-frequency and low-frequency fringes.

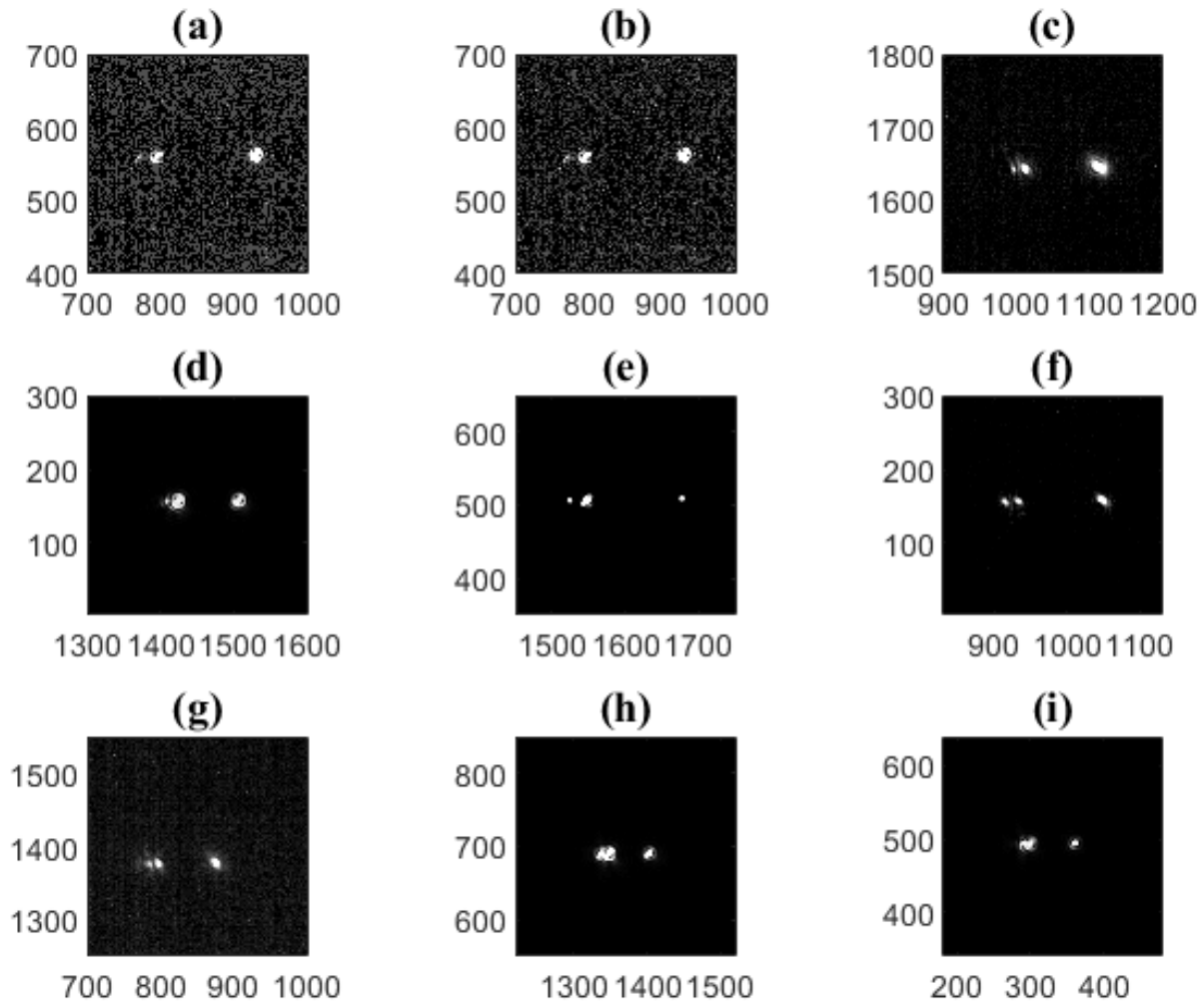

Figure 11 : glare points of nine different droplets (noted (a) to (i)) recorded with the in-focus imaging line.

Particle	d_{BD} (µm)	d_{AB} (µm)	d_{AB}/d_{BD}
a	198	166	0.84
b	198	168	0.85
c	149	127	0.85
d	124	104	0.84
e	194	166	0.86
f	170	146	0.86
g	113	99	0.88
h	86	74	0.85
i	90	77	0.86

Table 1 : inter- glare points distances for the nine droplets (a) to (i) of figure 11. (Glare points A, B and D are those represented schematically on figure 2)

Figure 12 shows finally the in-focus images of three water droplets before contrast enhancement ((a), (b) and (c)) and after contrast enhancement of the same images ((d), (e) and (f) respectively). They show cases where the intensity of glare point B is very low. Cases (a) and (b) are comparable to the case discussed in figures 9 and 10. Case (c) is the one discussed in figures 7 and 8. So two cases induce an important underestimation of the size of the droplet in ILIDS (cases (a) and (b)), while the last one (case (c)) can be well processed.

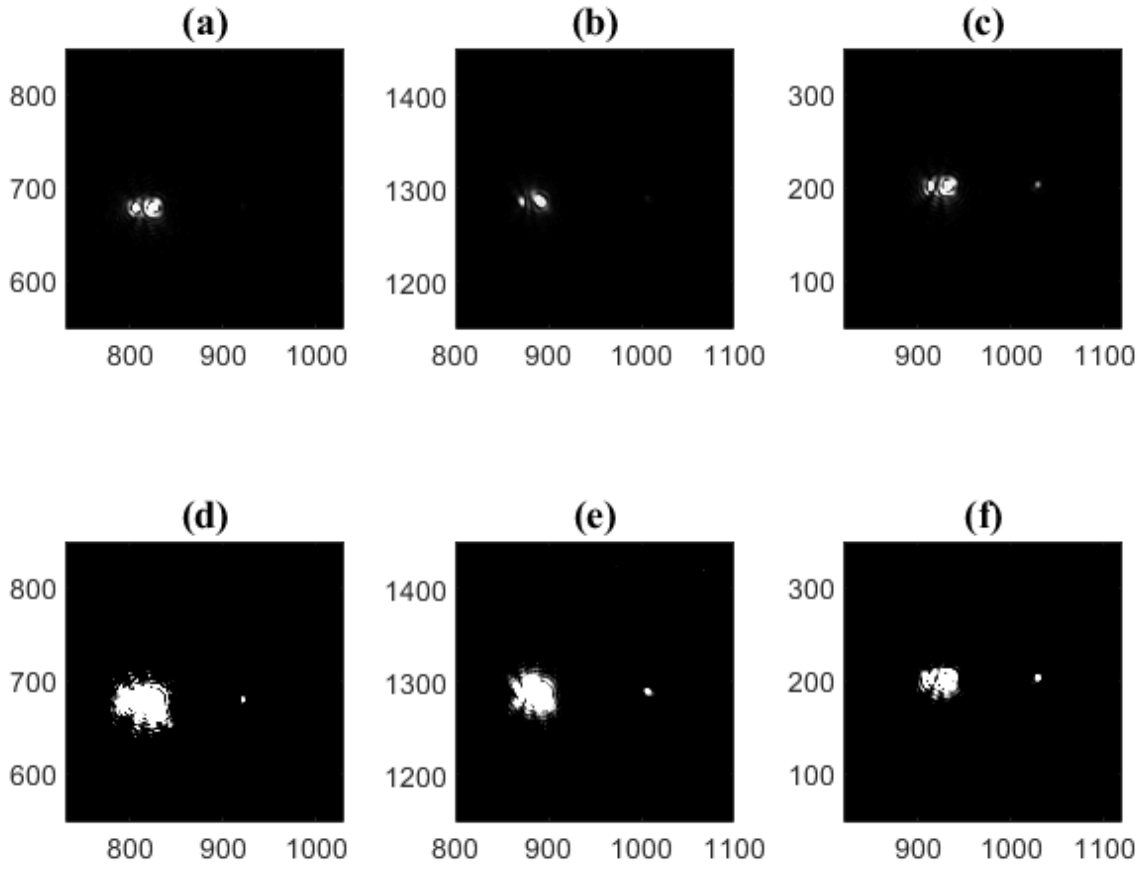

Figure 12 : glare points of three droplets recorded with the in-focus imaging line : without contrast enhancement (a) to (c) ; and after contrast enhancement of the same images : (d) to (e) respectively.

4.4. Discussion

These experimental results bring very important information. Some of them can be in contradiction with the theoretical part (see figure 2 which illustrates the location on the droplet surface of glare points A, B, C and D):

- experimentally, the intensity of p=3 scattering order is not negligible and can become comparable to the intensity of other orders p=0 and p=1. For example figure 11(f) shows

clearly a case where glare points A and D exhibit comparable intensities. This was predicted theoretically, but not expected with such a regular occurrence. The size of the aperture of the imaging system, the transverse position of the droplet in the field of view, and the uncertainties concerning the scattering angle are parameters that can explain the relatively high intensity of p=3 scattering order that is frequently observed. The ILIDS image has thus to be analyzed correctly considering that it is a three-wave interference pattern. A systematic error of 15% in the size determination of the droplet can occur if the fringe frequencies measured are not attributed correctly to the corresponding glare points. In our results, we did not encounter cases where glare points A and C could be separated.

- in rare cases, the intensity of glare point B is so low that the sole glare points observable are A and D. The fringe frequency analysis leads then to a dramatic underestimation of the size of the droplet (figures 9 and 10). A lower intensity of glare point B was predicted theoretically in some cases (see figure 3), but not in such a proportion that glare point B can almost disappear. This latter observation is not easily justified theoretically. A first explanation is linked to the longitudinal position of the droplets in the laser sheet illuminating the volume of interest. When droplets are on the border of the laser sheet, glare point B (depending on the part of the droplet that is not in the sheet anymore) could exhibit a lower intensity.

Figure 13 shows then scattering diagrams predicted using exact Lorenz-Mie theory. Figure 13(a) shows the scattered intensity versus the scattering angle θ for a water droplet of radius 15μm. Figure 13(b) shows the scattered intensity versus θ for a water droplet of radius 80μm. Interference patterns are fairly complicated. For r = 15μm, high-frequency oscillations of about one cycle per degree, with a low-frequency envelope of about roughly one cycle every 7° are observed. For r = 80μm, a well-contrasted high frequency oscillation of about 5 cycles per degree is observed as long as $\theta < 90°$. But for higher scattering angles, the contrast of this high-frequency component is much reduced while a lower-frequency component of about 1 cycle per degree exhibits a much higher contrast. There is then a possible ambiguity in pattern interpretation if the high-frequency component is covered by the noise of the experiment when $90° < \theta < 95°$, as observed in the special case of section 4.2. This is a second theoretical cause to the possible underestimation of the droplets' size that can sometimes occur.

In summary, on this panel of twelve droplets (figures 11 and 12), a dramatic underestimation of the droplet's size will be done in two cases (cases (a) and (b) of figure 12) when the intensity of p=1 scattering is very low (glare point B). An analysis in terms of three-wave interference patterns (generated by spots A, B and D) leads to a correct estimation of the droplet's size in eight cases. But with this procedure, an underestimation of 15% of the droplet's size can occur in two cases (cases (a) and (b) of figure 11) if the intensity of glare point D is so low that it does not contribute to the pattern. The ILIDS image corresponds then to a two-wave interference pattern produced by the traditional glare points A and B.

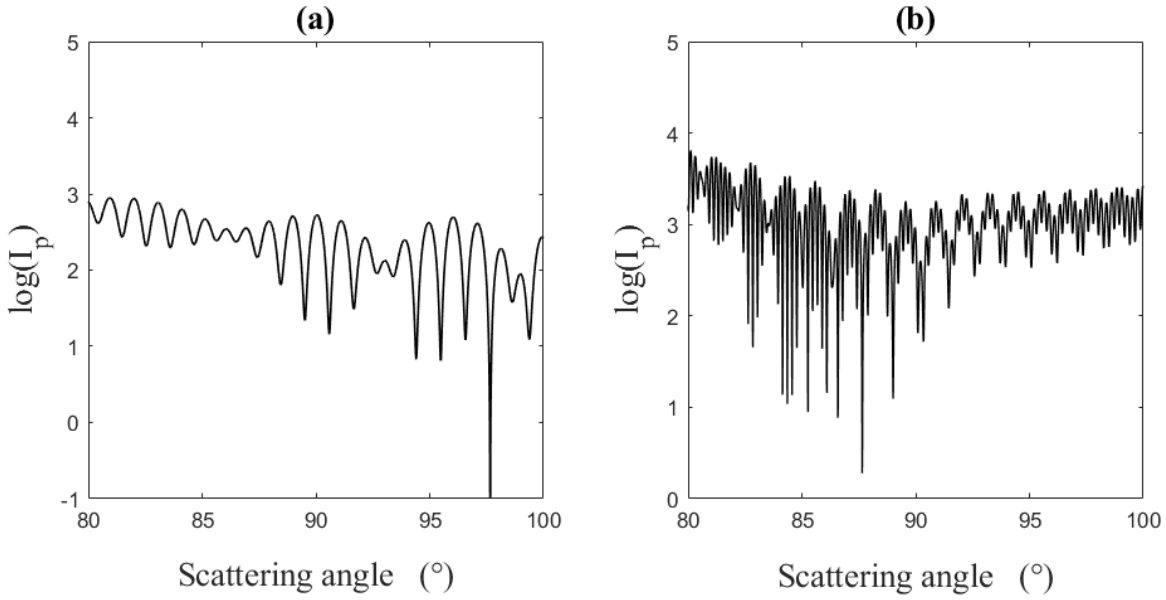

Figure 13 : Scattered intensity versus the scattering angle θ using Mie theory for water droplets of radii 15 μm (a) and 80 μm (b).

ILIDS is traditionally interpreted in terms of two glare points on the surface of a droplet that generate a two-waves interference pattern. If this assumption is well-satisfied at θ = 67° for a perpendicular polarization of the laser light, it appears that the interpretation of the interferometric images can be much more complicated at θ = 90° for a parallel polarization of the laser light. In many cases, results can be interpreted by the presence of a third glare point D due to p=3 scattering. But experimental results show that some rare cases of erroneous size determination exist. Exact Lorenz-Mie calculations confirm that the behaviors encountered are fairly complicated. Adding experimental noise, the interpretations can become uncertain in the case of low-contrasted fringes.

Our results indicate that it would be interesting to avoid measurements at scattering angles where p = 3 waves are important. Unfortunately, the combination of all parameters (size range of the droplets to be measured, aperture of the imaging system, position of the droplet in the field of view and thus range of scattering angles to be considered for each droplet depending on his position), tends to make such an optimization very complex.

5. Conclusion

In conclusion, our results show that the presence of a third glare point can not be neglected in ILIDS when the scattering angle is 90° (with a parallel polarization of the laser light). Experiments show that glare point D due to p=3 scattering, which involves surface waves, exhibits a relatively high intensity. An interpretation of the interference patterns in terms of three wave interferences leads to an accurate estimation of the droplet's size in most cases. Nevertheless, in a few cases (17% during our experiments), an unexpected low-intensity of the glare point attributed to p=1 scattering leads to a strong underestimation of the size of

the droplet. We explain this error by the potential location of the measured droplet at the border of the illumination laser sheet. These observations are of great importance for the design of embedded instruments to be used in wind tunnels or cloud chambers, applied to airborne applications or the wide variety of known applications [26-31]. New configurations could be interesting [32] and accurate image processing algorithms need to be developed and optimized [33,34].

Acknowledgments

Authors wish to thank the reviewers for their very fruitful reports.

This work is supported by Region Normandy for CPER and European Union for FEDER project "THESIS".

References

[1] G. König, K. Anders, A.Frohn, J.Aerosol Sci. 17 (1986) 157.
[2] R. Ragucci, A. Cavaliere, P. Massoli, Part. Part. Syst. Charact. 7 (1990) 221.
[3] K.H. Hesselbacher, K. Anders, A.Frohn, Appl. Opt. 30 (1991) 4930-4939.
[4] A.R. Glover, S.M. Skippon, R.D. Boyle, Appl. Opt. 34 (1995) 8409.
[5] N. Damaschke, H. Nobach, C. Tropea, Exp. Fluids 32 (2002) 143-152.
[6] H.E. Albrecht, M. Borys, N. Damaschke, C. Tropea (2003). Laser Doppler and Phase Doppler measurement techniques. Springer Verlag, Berlin.
[7] S. Dehaeck, J. van Beeck, and M. Riethmuller, Exp. Fluids 39 (2005) 407-419.
[8] S. Dehaeck and J. P. A. P. Van Beeck, Exp. Fluids 42 (2007) 767-781.
[9] S. Dehaeck, J.P.A. van Beeck, Exp. Fluids 45 (2008) 823-831.
[10] H. Shen, S. Coetmellec, G. Grehan, M. Brunel, Appl. Opt. 51 (2012) 5357.
[11] H. Shen, S. Coetmellec, M. Brunel, Opt. Lett. 37 (2012) 3945.
[12] E. Porcheron, P. Lemaitre, J. van Beeck, R. Vetrano, M. Brunel, G. Gréhan, L. Guiraud, J. Europ. Opt. Soc.: Rap. Public 10 (2015), 15030.
[13] J. Jacquot-Kielar, Y. Wu, S. Coëtmellec, D. Lebrun, G. Gréhan, M. Brunel, J. Quant. Spectrosc. Radiat. Transf. 178 (2016) 108-116.
[14] M. Brunel, S. Coëtmellec, G. Gréhan, H. Shen, J. Europ. Opt. Soc. Rap. Public. 9 (2014) 14008.
[15] M. Brunel, S. Gonzalez Ruiz, J. Jacquot, J. van Beeck, Opt. Commun. 338 (2015) 193-198.
[16] H.C. van de Hulst, R.T. Wang, Appl. Opt. 30 (1991) 4755.
[17] M. Brunel, M. Talbi, S. Coetmellec, G. Gréhan, Y. Wu, J. Jacquot, Opt. Commun. 433 (2019) 173-182.
[18] E.A. Hovenac, J.A. Lock, J. Opt. Soc. Am. A 9 (1992) 781-795.
[19] C. Mounaïm-Rousselle, O. Pajot, Part. Part. Syst. Charact. 16 (1999) 160-168.
[20] C. Lacour, D. Durox, S. Ducruix and M. Massot, Exp. Fluids 51 (2011) 295-311.
[21] J. Jacquot-Kielar, P. Lemaitre, C. Gobin, Y. Wu, E. Porcheron, S. Coëtmellec, G. Gréhan, M. Brunel, Opt. Commun. 372 (2016) 185-195.
[22] W.J. Glantschnig, S.H. Chen, Appl. Opt. 20 (1981) 2499.
[23] http://www.philiplaven.com/mieplot.htm

[24] J.A. Lock, P. Laven, J. Opt. Soc. Am. A 28 (2011) 1086-1095.
[25] L. Ouldarbi, G. Pérret, P. Lemaitre, E. Porcheron, S. Coëtmellec, G. Gréhan, D. Lebrun, M. Brunel, Applied Optics 54 (2015) 7773-7780.
[26] R. S. Volkov, G. V. Kuznetsov and P. A. Strizhak, Int. J. Heat Mass Transfer 96 (2016) 20-28.
[27] R. S. Volkov, S. V. Chvanov, D. D. Andriyanov, Techn. Phys. Lett. 46 (2019) 605-608.
[28] Y. Wu, H. Li, M. Brunel, J. Chen, G. Gréhan, L. Madler, Appl. Phys. Lett. 111 (2017) 041905.
[29] H. Zhang, M. Zhai, J. Sun, Y. Zhou, D. Jia, T. Liu and Y. Zhang, J. Quant. Spectrosc. Radiat. Transfer 187 (2017) 62-75.
[30] H. Zhang, Y. Zhou, J. Liu, D. Jia, T. Liu, Rev. Scient. Inst. 88 (2017) 043302.
[31] J. Sun, H. Zhang, X. Wang, D. Jia, T. Liu, M. Zhai, Opt. Exp. 26 (2018) 14097-14107.
[32] Y. Wu, Z. Lin, X. Wu, K. Cen, Powder Technol. 356 (2019) 31-38.
[33] L. Qieni, J. Wenhua, L. Tong, W. Xiang, Z. Yimo, Opt. Commun. 312 (2014) 312.
[34] L. Qieni, Y. Xiaoxue, G. Baozhen, C. Tingting, Opt. Exp. 26 (2018) 1038-1048.

Figure Captions

Figure 1 : intensity of scattering orders p=0 to p=7 versus the scattering angle θ for a droplet of radius 80 μm. (The intensity of order p=2 is lower and does not appear).

Figure 2 : schematic representation of the three glare points A, B and C corresponding to the scattering orders p=0, p=1 and p=3.

Figure 3 : intensity of scattering orders p=0, p=1 and p=3 versus the scattering angle θ for droplets of radii 15 μm (a) and 80 μm (b).

Figure 4 : range of scattering angles to be considered depending on the position of the droplet in the field of view. Two cases are illustrated here : droplet over the optical axis (range $[\theta_{1min}; \theta_{1max}]$), or below the optical axis (range $[\theta_{2min}; \theta_{2max}]$).

Figure 5 : intensity of scattering orders p=0 (star), p=1 (cross) and p=3 (circles) versus the droplet's radius. In black, the intensity has been integrated over the range of scattering angles [87°,93°]. In red, the intensity has been integrated over the range of scattering angles [93°,99°].

Figure 6 : experimental set-up : (a) side-view, (b) top view.

Figure 7 : interferometric out-of-focus image of a droplet (a) and horizontal line of the interferogram (b)

Figure 8 : glare points of the droplet whose defocused image is reported in figure 7(a), without contrast enhancement (a) and after contrast enhancement (b).

Figure 9 : : interferometric out-of-focus image of a droplet (a) and horizontal line of the interferogram (b)

Figure 10 : glare points of the droplet whose defocused image is reported in figure 7(a), without contrast enhancement (a) and after contrast enhancement (b).

Figure 11 : glare points of nine different droplets (noted (a) to (i)) recorded with the in-focus imaging line.

Figure 12 : glare points of three other droplets recorded with the in-focus imaging line : without contrast enhancement (a) to (c) ; and after contrast enhancement of the same images : (d) to (e) respectively.

Figure 13 : Scattered intensity versus the scattering angle θ using Mie theory for water droplets of radii 15 μm (a) and 80 μm (b).